



High-Nuclearity Polyoxometalate-Based Metal–Organic Frameworks for Photocatalytic Oxidative Cleavage of C–C Bond

Qixin Zhao⁺, Yang Zeng⁺, Zhiqiang Jiang, Zhenxuan Huang, De-Liang Long, Leroy Cronin,^{*} and Weimin Xuan^{*}

Abstract: High-nuclearity polyoxometalate (POM) clusters are attractive building blocks (BBs) for the synthesis of metal–organic frameworks (MOFs) due to their high connectivity and inherently multiple metal centers as functional sites. This work demonstrates a strategy of step-wise growth on ring-shaped $[P_8W_{48}O_{184}]^{40-}$ precursor, which produced two new high-nuclearity polyoxotungstates, a half-closed $[H_{16}P_8W_{58}O_{218}]^{32-}$ $\{W_{58}\}$ and a fully-closed $[H_{16}P_8W_{64}O_{236}]^{32-}$ $\{W_{64}\}$. By in situ synthesis, unique MOFs of copper triazole-benzoic acid (HL) complexes incorporating the negatively-charged $\{W_{58}\}$ and $\{W_{64}\}$ as nodes, $[Cu_{11}(HL)_9W_{58}]$ **HNPOMOF-1** and $[Cu_9(HL)_9W_{64}]$ **HNPOMOF-2**, were constructed by delicately tuning the reaction conditions, mainly solution pH, which controls the formation of $\{W_{58}\}$ and $\{W_{64}\}$, and at the same time the protonation of triazole-benzoic acid ligand thus its coordination mode to copper ion that creates the highest nuclearity POM-derived MOFs reported to date. **HNPOMOF-1** features 3D framework possessing cage-like cavities filled with exposed carboxyl groups, while the inherent 2D layer-like **HNPOMOF-2** allows for facile exfoliation into ultrathin nanosheets, and the resulted **HNPOMOF-2_{NS}** exhibits superior activity towards photocatalytic oxidative cleavage of C–C bond for a series of lignin models. This work not only provides a strategy to build high-nuclearity POM cluster-based frameworks, but also demonstrates their great potential as functional materials for green catalysis.

Introduction

Polyoxometalates (POMs) are a class of anionic clusters constructed from early transition metal-oxo units (Mo, W, V, Nb, Ta) and show a wide range of applications in the fields of chemistry and material science due to their strong acidity, reversible multi-electron redox behavior and photo/electro-responsive properties.^[1] POMs in general possess rigid and anionic skeleton lined with abundant surface oxygen atoms, these characteristics facilitate their use as functional building blocks (BBs) for constructing crystalline materials through coordination, hydrogen bonding, and electrostatic interactions.^[2] As an archetypal cyclic cluster, $[P_8W_{48}O_{184}]^{40-}$ ($\{P_8W_{48}\}$) features a large cavity (diameter: approximately 10 Å) built from condensation of four six-vacant $[P_2W_{12}O_{48}]^{14-}$ subunits and plenty of oxo sites both within the internal cavity and on external surface, providing an ideal platform for incorporating additional metal sites to build functional assemblies.^[3] Moreover, $\{P_8W_{48}\}$ exhibits high chemical stability across a wide pH range (1–8).^[4] Therefore, binding metal ions to the internal oxo sites of $\{P_8W_{48}\}$ has led to a series of cluster-in-cluster aggregates, exemplified by $\{V_{12}\}@\{P_8W_{48}\}$, $\{Fe_{16}\}@\{P_8W_{48}\}$, $\{Al_{16}\}@\{P_8W_{48}\}$, $\{Ga_{16}\}@\{P_8W_{48}\}$, $\{Cu_{16}\}@\{P_8W_{48}\}$, $\{Cu_{20}\}@\{P_8W_{48}\}$ and $\{Ag_{30}\}@\{P_8W_{48}\}$,^[5] while coordination with external/surface oxo ligands facilitates the formation of 1D to 3D pure inorganic frameworks such as $\{Mn_8P_8W_{48}\}_n$, $\{Ag_4P_8W_{48}\}_n$ and $\{Co_{10}P_8W_{48}\}_n$ (Figure 1a).^[6] These $\{P_8W_{48}\}$ -derived clusters and frameworks have demonstrated diverse applications, ranging from proton conduction to catalysis.^[5c,d,f]

Metal–organic frameworks (MOFs) have emerged as a prototypical class of crystalline, porous materials built from metal ions/metal clusters and organic ligands.^[7] MOFs are well known for their high porosity, structure tunability and diverse functionality, enabling wide applications from fundamental science to industry.^[7c,8] Typically, POMs can either combine with metal ions as BBs or act as anion templates to construct POM-based metal–organic frameworks (POMOFs).^[9] Reflecting the structural diversity of POMs, a vast array of POMOFs have been produced from various POM clusters with different nuclearities, charges and shapes.^[10] Nonetheless, high-nuclearity polyoxometalate-based metal–organic frameworks (HNPOMOFs) constructed from POM clusters containing metal sites > 50 remain scarce. Focusing on polyoxotungstates (POTs), most reported POMOFs utilize low-nuclearity clusters such as $\{W_6\}$, $\{W_{10}\}$, $\{XW_{12}\}$ (X=P, Si, B, etc.) and $\{P_2W_{18}\}$ (Figure 1b).^[11] To the best of our knowledge, $\{P_5W_{30}\}$ represents

[*] Q. Zhao,⁺ Y. Zeng,⁺ Z. Jiang, Z. Huang, Prof. W. Xuan
 State Key Laboratory for Modification of Chemical Fibers and Polymer Materials, College of Chemistry and Chemical Engineering, Donghua University
 Shanghai 201620, P. R. China
 E-mail: weiminxuan@dhu.edu.cn

Dr. D.-L. Long, Prof. L. Cronin
 School of Chemistry, The University of Glasgow, Glasgow G12 8QQ, UK
 E-mail: lee.cronin@glasgow.ac.uk

[†] These authors contributed equally to this work.

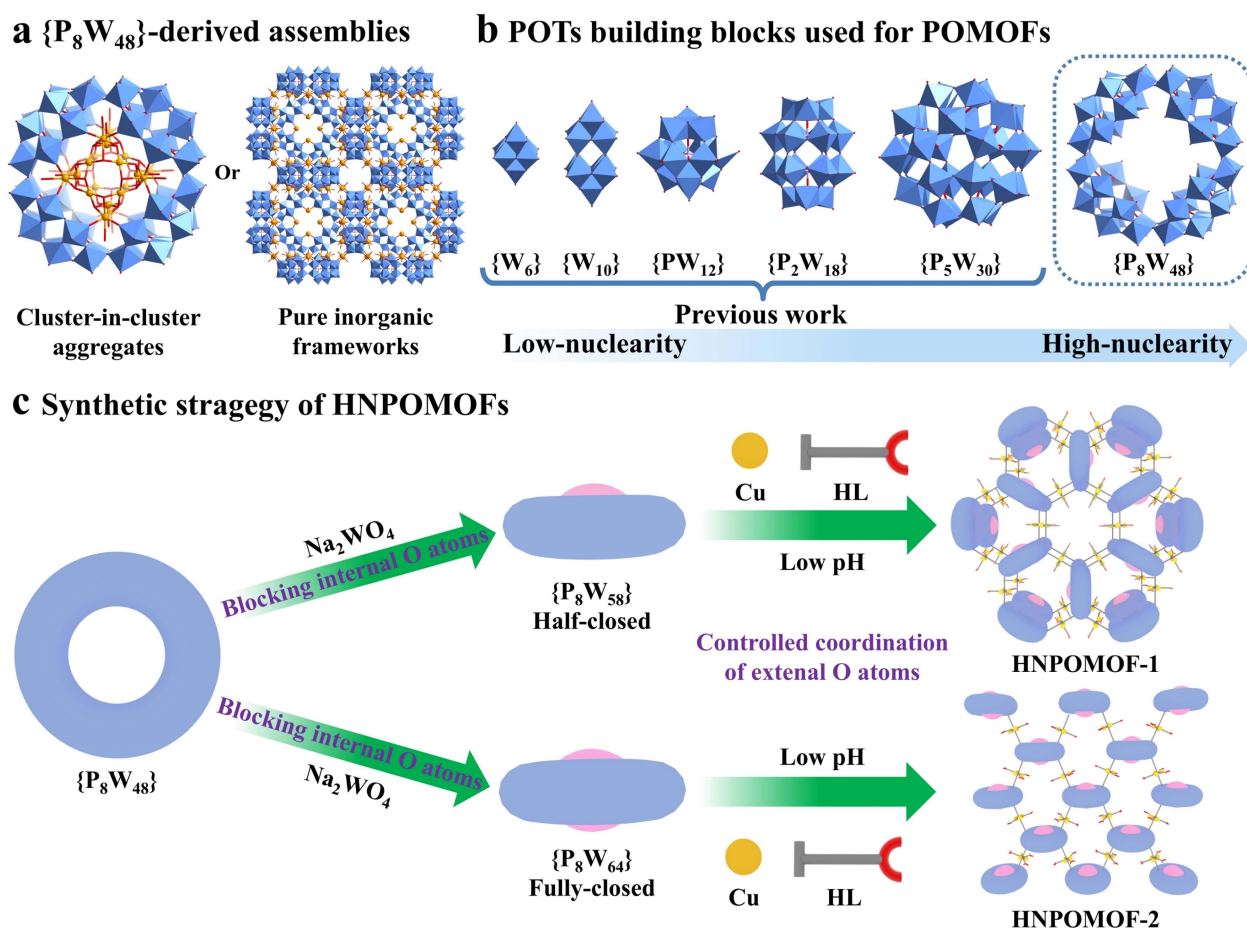


Figure 1. (a) $\{P_8W_{48}\}$ -derived assemblies including cluster-in cluster aggregates and pure inorganic frameworks. (b) POTs building blocks used for POMOFs, with nuclearity increasing from $\{W_6\}$ to $\{P_5W_{30}\}$. (c) Demonstration of the synthetic strategy of HNPOMOFs using $\{P_8W_{48}\}$ as precursor via controlling the reactivity of both internal and external oxo ligands.

the highest nuclearity POT employed in POMOF synthesis (Figure 1b).^[12] In MOF chemistry, high nuclearity clusters, including $\{Zr_{16}\}$, $\{Al_{24}\}$, $\{Ln_{26}/\{Ln_{48}\}$ ($Ln=Er, Dy, Ho, Gd$), $\{Ag_{27}\}$ and $\{Ag_{72}\}$, have been explored as nodes to expand MOF diversity, and the collective effect from polynuclear metal sites endow them with unique physicochemical properties.^[13] Compared to these BBs, using high-nuclearity POMs to synthesize HNPOMOFs presents a great challenge due to their inherently high negative charges and strong interactions with metal ions. Upon introduction of organic ligands, the concurrent coordination to metal ions will cause quick assembly and thus easily result in amorphous solids rather than crystalline frameworks.

To overcome the current limitation, we aim to employ $\{P_8W_{48}\}$ as precursor to explore the synthesis of HNPOMOFs given its facile tunability, diverse functionality and high stability. Addressing the aforementioned challenges requires controlling the reactivity of $\{P_8W_{48}\}$ (Figure 1c).^[6b] We propose two potential strategies: (1) Blocking the internal oxo sites of $\{P_8W_{48}\}$ from building heterometal cluster by sealing its internal cavity with additional W atoms, thereby limiting the number of metal ions available for assembly with ligands. Meanwhile, the blocking of reactive

internal oxo sites will also improve the stability of parent $\{P_8W_{48}\}$. (2) Conducting the synthesis at low pH value. The presence of high concentration of H^+ ions can compete with metal ions to interact with the external oxo sites on $\{P_8W_{48}\}$ while simultaneously suppressing the interaction of N/O donors on ligands with metal sites. This will reduce the coordination tendency of external POM oxo ligands to metal ions and decelerate the coordination rate between ligands and metal ions, thereby facilitating the ordered assembly of all components into crystalline and periodic frameworks (Figure 1c). On the other hand, judicious choice of metal ions and ligands is also crucial in constructing POMOFs with desired structures and functionalities. Copper ions are well-known for their diverse coordination geometries, ranging from tetrahedral to octahedral configurations, and their critical roles in enhancing photocatalytic activity and extending the absorption to visible region.^[11,14] Triazole-benzoic acid ligand can facilitate assembly with copper ions to generate stable dinuclear and trinuclear Cu-based secondary building units, which are conducive to building porous POMOFs with open channels.^[15] The rational combination of copper ions, triazole-benzoic acid and $\{P_8W_{48}\}$ is therefore

promising for achieving robust, porous and functional HNPOMOFs.

Herein we report the synthesis of two novel POMs $\{P_8W_{58}\}$ and $\{P_8W_{64}\}$ based MOFs, **HNPOMOF-1** and **HNPOMOF-2**, by controlling the reactivity of $\{P_8W_{48}\}$ upon assembly with Cu^{2+} ion and 4-(4'-carboxyphenyl)-1,2,4-triazole (**HL**) ligand in the presence of additional sodium tungstate (Figure 1c). Notably, **HNPOMOF-2** represents the highest nuclearity POM-derived MOF reported to date. The introduction of sodium tungstate enables the in situ growth of add-on $\{W_8\}$ and $\{W_1\}$ units on $\{P_8W_{48}\}$, resulting in either half-closed $[H_{16}P_8W_{58}O_{218}]^{32-}$ $\{P_8W_{58}\}$ or fully-closed $[H_{16}P_8W_{64}O_{236}]^{32-}$ $\{P_8W_{64}\}$ (Figure 1c). By blocking the internal oxo sites, these two expanded $\{P_8W_{48}\}$ derivatives allow for the assembly of **HNPOMOF-1** and **HNPOMOF-2** featuring 3D and 2D frameworks, respectively, under very low pH value. The strong acidic synthesis condition not only depresses the reactivity of external oxo ligands on $\{P_8W_{58}\}$ and $\{P_8W_{64}\}$, but also keeps the carboxyl groups on **HL** ligands in **HNPOMOF-1** and **HNPOMOF-2** remaining protonated. Upon exfoliation of **HNPOMOF-2** into ultra-thin single layers, the **HNPOMOF-2_{NS}** demonstrates enhanced catalytic performance in the photocatalytic oxidation of lignin models compared to **HNPOMOF-1** and pristine **HNPOMOF-2**, due to the more accessible active sites and faster diffusion of substrate/product. This work demonstrates controlling the reactivity of POM clusters can be potentially developed as a general approach, which can greatly extend the structural library and application of high-nuclearity cluster-based functional assemblies.

Results and Discussion

Synthesis and Characterization

HNPOMOF-1 and **HNPOMOF-2** have compositions of $K_2NaH_{10}[Cu_{11}(OH)(C_9H_6N_3O_2)(C_9H_7N_3O_2)_8(H_2O)_{20}][H_{16}P_8W_{58}O_{218}] \cdot 120H_2O$ and $K_4Na_{10}H_2[Cu_9(OH)(C_9H_7N_3O_2)_9(H_2O)_{22}][H_{16}P_8W_{64}O_{236}] \cdot 97H_2O$ established by structure determinations and chemical analyses. They were facilely synthesized via one-pot reaction of $CuSO_4$, **HL**, $K_{28}Li_5[H_7P_8W_{48}O_{184}] \cdot 92H_2O$ and Na_2WO_4 under hydrothermal conditions. The addition of Na_2WO_4 is essential for providing additional tungstate source and tuning the reactivity of $\{P_8W_{48}\}$ in the formation of **HNPOMOF-1** and **HNPOMOF-2**, as unidentified crystalline precipitates are always obtained in the absence of Na_2WO_4 under the same conditions. This is likely due to the high reactivity of pristine $\{P_8W_{48}\}$. In some cases, pure 1D inorganic framework $\{Cu_9P_8W_{48}\}_n$, where 8 Cu^{2+} ions are entrapped within the cavity of $\{P_8W_{48}\}$, can be isolated from the filtrate after removing precipitate (Figure S9). This further indicates the importance of blocking the internal oxo sites of $\{P_8W_{48}\}$. By introducing sodium tungstate during assembly, it can condense with the internal O atoms of $\{P_8W_{48}\}$ and thus reduce the reactivity via the in situ generation of half-closed $\{P_8W_{58}\}$ or full-closed $\{P_8W_{64}\}$. Moreover, tungstate can behave as anionic ligand to

compete with the external O atoms on $\{P_8W_{58}\}/\{P_8W_{64}\}$, thereby weakening the interaction between copper ions and $\{P_8W_{58}\}/\{P_8W_{64}\}$. Another key factor affecting the self-assembly is pH value. Performing the synthesis at $pH > 1.5$ in generally resulted in amorphous solid and sometimes $\{P_2W_{18}\}$ -based POMOFs due to the fast coordination of $\{P_8W_{58}\}/\{P_8W_{64}\}$ and **HL** to copper ions or decomposition of $\{P_8W_{48}\}$ at relatively high pH values. In contrast, when the pH was adjusted below 1, the clear solution was produced rather than crystals. This is caused by complete depression of the coordination abilities of both surface oxo ligands on POM BBs and N/O donors on **HL**. Overall, the successful assembly of **HNPOMOF-1** and **HNPOMOF-2** is tuned by delicate control of the reactivity of POM BBs and ligands.

HNPOMOF-1 crystallizes in the *R*-3c space group, and the asymmetric unit contains half $\{P_8W_{58}\}$, five and half Cu ions, four **HL** and half deprotonated **L**, and K^+ counterions (Figure S3). $\{P_8W_{58}\}$ can be viewed as a half-closed cluster based on $\{P_8W_{48}\}$, with one side sealed by $\{W_8\}$ add-on unit while two $\{W_1\}$ units located on the vacant sites between adjacent $\{P_2W_{12}\}$ subunits on the other side (Figure 2a and Figure S4). The five and half Cu ions can be divided into three types according to their coordination modes. The first type, half occupied Cu1, adopts a coordination environment of distorted tetrahedron and occupies the vacancy between adjacent $\{P_2W_{12}\}$ subunits to afford $\{Cu_2P_8W_{58}\}$ (Figure 2b). Upon coordination of triazoles on three ligands to Cu2, Cu3, and Cu4, a classical trinuclear $\{Cu_3(\mu_3-OH)(HL)_3\}$ unit is generated (Figure 2c).^[16] All the three Cu ions are in six-coordinated octahedral geometry. Moreover, Cu5 and Cu6 also adopt octahedral configuration and link with one **HL** and half **L** to construct $\{Cu_2(\mu_2-O)(HL)L_{0.5}\}$ unit (Figure 2c). Owing to the disorder of **L** at two equivalent positions, it can either use triazole or carboxylate coordinating to dinuclear Cu centers (Figure 2c).

As such, two $\{Cu_2(\mu_2-O)(HL)L_{0.5}\}$ units link with each other forming a dimer, which further connects with adjacent $\{Cu_2P_8W_{58}\}$ clusters via external oxo ligands, resulting in an infinite zig-zag chain along the *c*-axis (Figure S5). Six 1D chains associate in parallel constituting the wall of a hexagonal tubule with an opening size of $13.9 \text{ \AA} \times 13.9 \text{ \AA}$ (Figure 2d). Furthermore, the neighboring chains can be further linked by $\{Cu_3(\mu_3-OH)(HL)_3\}$ units, creating a 3D framework featuring 1D hexagonal channels filled by **HL** ligands with exposed carboxyl groups pointing to each other (Figure 2e). These uncoordinated carboxyl ligands are regulated by 3-fold rotary inversion axis and thus arrange in groups of three **HL**, which truncate the 1D open channels into two types of cage-like cavities showing diameters ~ 12.8 and 14.0 \AA , respectively (Figure 2e and Figure S6).

Upon doubling the amount of sodium tungstate, **HNPOMOF-2** was produced under the otherwise identical conditions. The presence of more tungstate enables blocking both sides of $\{P_8W_{48}\}$, leading to fully-closed $\{P_8W_{64}\}$ as basic BB (Figure 3a). In contrast to half-closed $\{P_8W_{58}\}$, the either side of $\{P_8W_{48}\}$ in $\{P_8W_{64}\}$ is sealed by one $\{W_8\}$ unit, respectively (Figure 3b and Figure S8). This thus further reduces the reactivity/connectivity of $\{P_8W_{64}\}$, resulting in the formation of 2D layer-like **HNPOMOF-2** (Figure 3d).

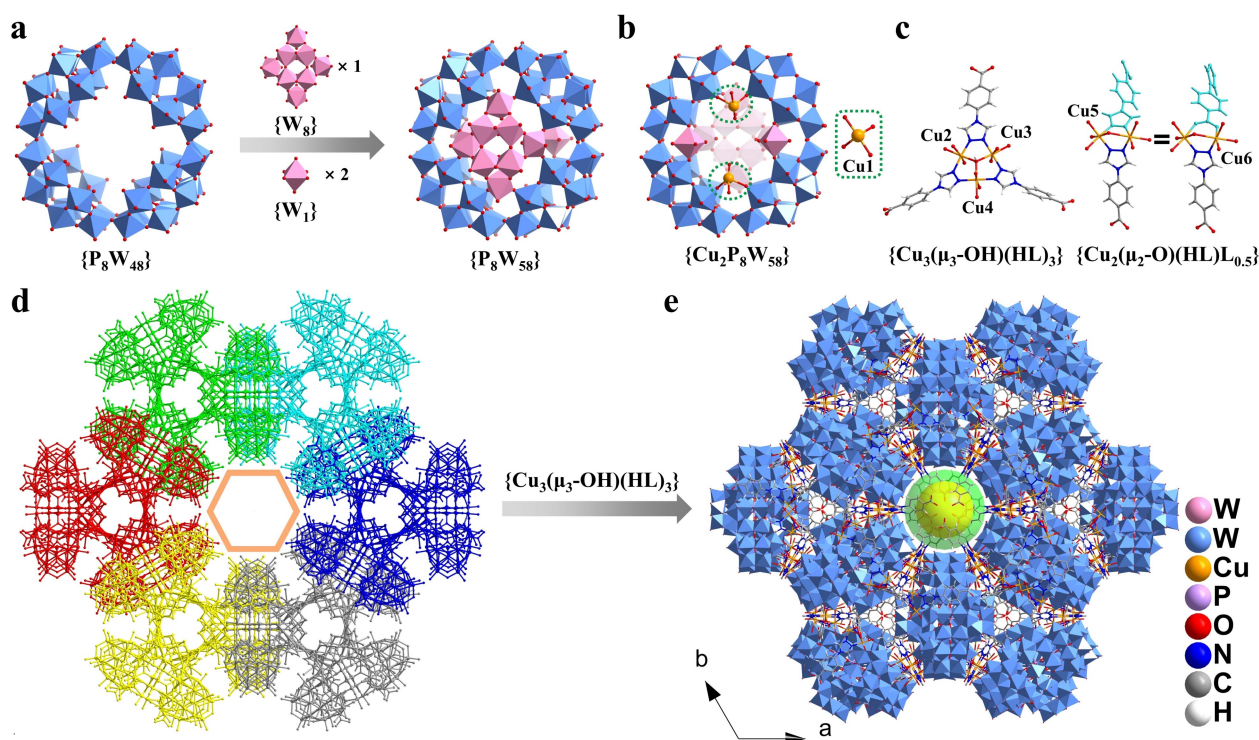


Figure 2. (a) Molecular structure of half-closed $\{P_8W_{58}\}$. (b) View of $\{Cu_2P_8W_{58}\}$ with one side capped by two tetrahedral Cu1. (c) View of the $\{Cu_3(\mu_3-OH)(HL)_3\}$ and $\{Cu_2(\mu_2-O)(HL)L_{0.5}\}$ units where L is disordered at two positions. The disorder L is highlighted in cyan. (d) Parallel association of six 1D chains constructed by $\{Cu_2(\mu_2-O)(HL)L_{0.5}\}$ and $\{Cu_2P_8W_{58}\}$ into a hexagonal tubule (orange). (e) 3D framework featuring 1D hexagonal channels along c-axis filled by exposed carboxyl groups, which truncate the channels into two types of cage-like cavities (yellow and green balls).

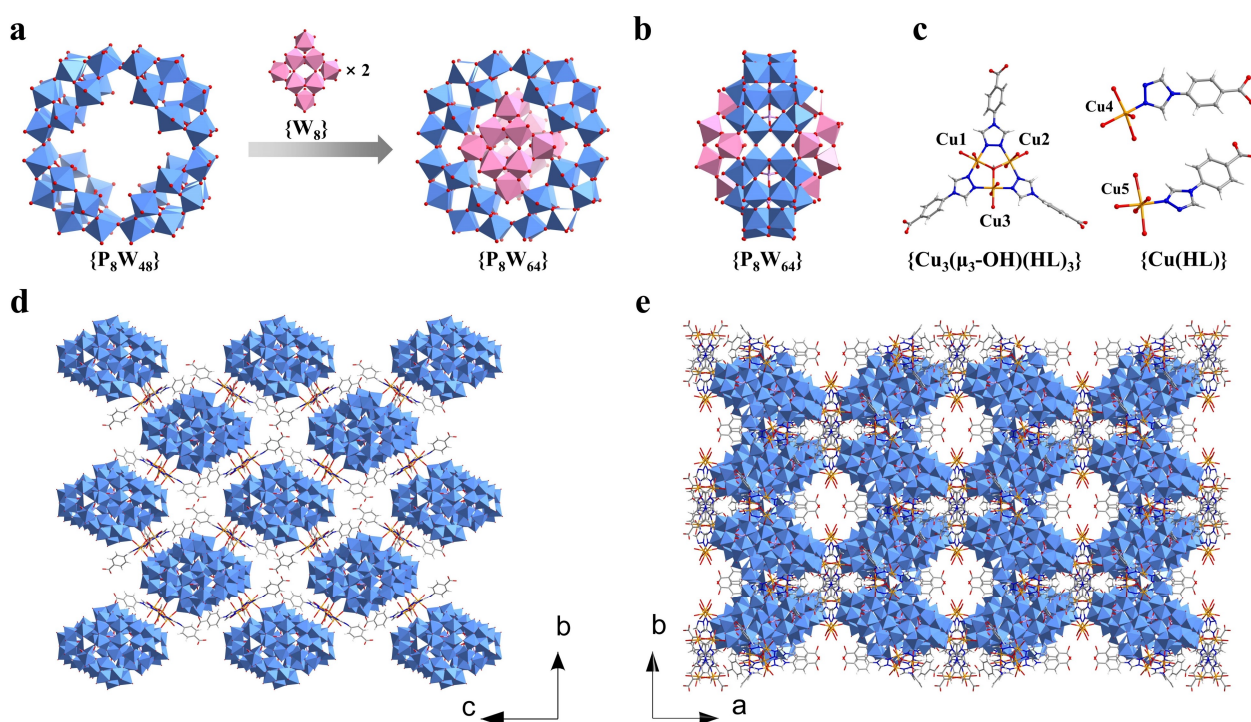


Figure 3. (a) Molecular structure of fully-closed $\{P_8W_{64}\}$. (b) Side view of $\{P_8W_{64}\}$. (c) $\{Cu_3(\mu_3-OH)(HL)_3\}$ and $\{Cu(HL)\}$ units. (d) 2D layer-like structure constructed from $\{P_8W_{64}\}$ and $\{Cu_3(\mu_3-OH)(HL)_3\}$ along b-c plane. (e) 3D supramolecular structure of HNPOMOF-2 along c-axis. Color Scheme is the same as Figure 2.

Compared with **HNPOMOF-1**, there are only $\{\text{Cu}_3(\mu_3\text{-OH})\text{-}(\text{HL})_3\}$ units present in the structure and behaving as 2-connected nodes to link with adjacent $\{\text{P}_8\text{W}_{64}\}$ along *b-c* plane (Figure 3c and 3d), while the other two types of $\{\text{Cu}(\text{HL})\}$ units show no connectivity and either attaches on the surface of $\{\text{P}_8\text{W}_{64}\}$ (Cu4 unit) or acts as counter cations (Cu5 unit) (Figure 3c). With the assistance of $\{\text{Cu}(\text{HL})\}$ units, a bundle of hydrogen bonds as well as electrostatic interaction are established between neighboring 2D layers, affording a 3D supramolecular structure containing microporous 1D channels of $5.9 \text{ \AA} \times 2.3 \text{ \AA}$ along *c*-axis (Figure 3e). These structural characteristics allows for potential exfoliation of **HNPOMOF-2** into 2D nanosheets.

The experimental PXRD patterns of **HNPOMOF-1** and **HNPOMOF-2** agree well with the simulated data, confirming their high phase purity (Figures S10 and S11). **HNPOMOF-1** and **HNPOMOF-2** exhibit good chemical stability, as evidenced by the excellent resistance towards aqueous solutions with a wide pH range (1–11) as well as boiling water and organic solvents such as acetonitrile for 24 h (Figures S13 and S14). Thermogravimetric analyses under N_2 atmosphere reveal that both compounds can be thermally stable up to $\sim 250^\circ\text{C}$ (Figures S17 and S18). Bond valence sum (BVS) calculations demonstrate all the W atoms adopt the valence state of +6 (Tables S3 and S5), while the Cu centers are in the mixed valence states, with a ratio of $\text{Cu}^{2+}/\text{Cu}^{1+}$ of 10:1 and 8:1 for **HNPOMOF-1** and **HNPOMOF-2**, respectively (Tables S2 and S4).^[17] The presence of Cu^{1+} sites is probably arisen from the reduction of Cu^{2+} by N-heterocyclic ligand under hydrothermal conditions.^[17] The same result is confirmed by the X-ray photoelectron spectroscopy (XPS) data where there only exists the signals corresponding to W^{6+} while the four peaks at 955.3, 952.2, 935.4, and 932.7 eV are consistent with the binding energies of $\text{Cu}(\text{II})\text{-}2_{\text{p}1/2}$, $\text{Cu}(\text{I})\text{-}2_{\text{p}1/2}$, $\text{Cu}(\text{II})\text{-}2_{\text{p}3/2}$, and $\text{Cu}(\text{I})\text{-}2_{\text{p}3/2}$, respectively, indicative of the presence of both $\text{Cu}(\text{II})$ and $\text{Cu}(\text{I})$ atoms in **HNPOMOF-1** and **HNPOMOF-2** (Figures S19–22). However, the ratios of $\text{Cu}^{2+}/\text{Cu}^{1+}$ deduced from XPS data are higher than those from BVS calculations. Time-dependent XPS measurement revealed that Cu^{2+} centers were gradually reduced upon X-ray irradiation and $\sim 80\%$ converted to Cu^{1+} sites after 60 min (Figure S23). We therefore attribute the discrepancy to the in situ reduction during XPS characterization, a phenomenon observed for other $\text{Cu}(\text{II})$ complexes.^[18]

Exfoliation of **HNPOMOF-2**

In view of the inherent 2D layer-like structure and weak interactions between adjacent layers, **HNPOMOF-2** was subjected to exfoliation by solvent-assisted liquid sonication using acetonitrile (Figure 4a).^[19] As shown by the scanning electron microscopy (SEM) imaging of the pristine crystals of **HNPOMOF-2**, the layered structure can be seen quite clearly (Figure 4b). Upon sonication for 72 h, **HNPOMOF-2** were successfully exfoliated into nanosheets, **HNPOMOF-2_{NS}**, as evidenced by the Tyndall effect upon irradiation of the colloid suspension with a laser beam (Figure 4c). TEM

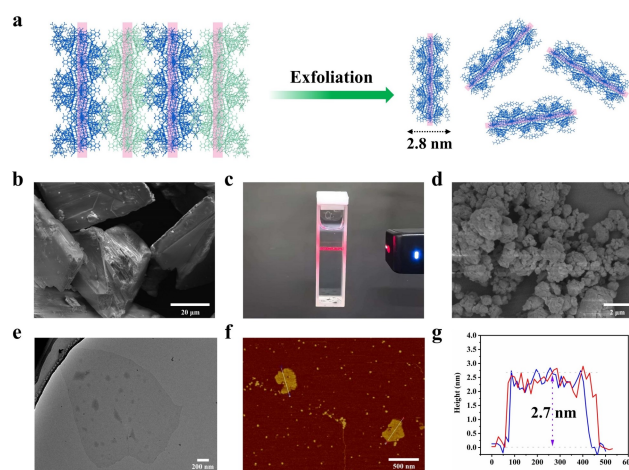


Figure 4. (a) Schematic diagram for the exfoliation of the bulk **HNPOMOF-2** to ultrathin 2D nanosheets. (b) SEM image of **HNPOMOF-2**. (c) The Tyndall effect of **HNPOMOF-2_{NS}** suspension in CH_3CN . (d) SEM image of **HNPOMOF-2_{NS}**. (e) TEM image of **HNPOMOF-2_{NS}**. (f) AFM image of **HNPOMOF-2_{NS}**. (g) Height of AFM image for the selective area.

analysis of **HNPOMOF-2_{NS}** revealed the ultrathin 2D nanosheets are in the size of $0.4 \times 0.7 \mu\text{m}^2$ (Figure 4e). AFM image further indicated the thickness of **HNPOMOF-2_{NS}** is about $2.7 \pm 0.2 \text{ nm}$, a value quite close to the theoretical thickness of monolayer (2.8 nm), implying that **HNPOMOF-2_{NS}** is composed of single layers (Figure 4f and 4g).

Photocatalysis

Lignin, an inedible component of lignocellulose, is the largest biomass feedback for production of value-added aromatics.^[20] The valorization of lignin in general involves selective cleavage of C–O or C–C linkages in monolignols.^[21] Since C–C bond has higher dissociation energy than that of C–O bond, the selective cleavage of C–C bond remains a great challenge.^[20,22] Photocatalysis has recently emerged as a powerful method for upgrading lignin into small platform chemicals.^[23] As a well-established type of photocatalyst, POM clusters such as decatungstate and transition metal-substituted POTs have demonstrated high-efficiency towards C–O cleavage.^[24] Nevertheless, the selective C–C bond cleavage was rarely reported by POM-based photocatalysts.^[25] To achieve this, the key point is to engineer the band structure of photocatalyst with proper conduction band and valence band energy that can guarantee sufficient redox capacity for C–C cleavage while keeping efficient light-harvesting ability.^[22] Due to the unique advantage by rational integration of POMs, metal centers and functional ligands into homogeneous frameworks, POMOFs exhibit modulable semiconductor characteristics favorable for photocatalysis.^[26] As such, the presence of photoactive POMs and transition metal sites in HNPOMOFs prompted us to explore their catalytic activities in

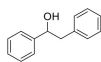
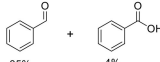
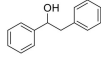
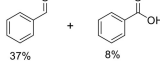
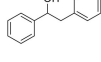
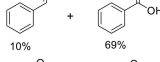
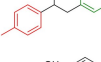
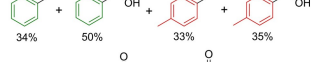
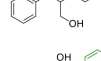
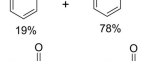
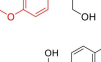
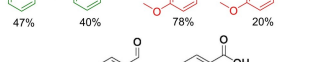
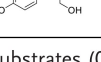
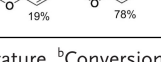
photocatalytic oxidative cleavage of C–C bond in lignin models.

Initially, 1,2-Diphenylethanol was selected as a model compound to investigate the photoactivity of **HNPO-MOF-1**, **HNPO-MOF-2** and **HNPO-MOF-2_{NS}**. Under the optimal conditions, all of them are capable of promoting the cleavage of C–C bond when 0.5 mol % catalyst was loaded to perform photooxidation in acetonitrile under the irradiation of 10 W 400 nm LED and atmosphere of air for 30 h (Table 1, entries 1–3). In all cases, the side product of 1,2-Diphenylethanone was hardly observed, indicating the reaction proceeded selectively via C_α–C_β bond cleavage rather than oxydehydrogenation of α-OH. Overall, the catalytic performance presents in the order of **HNPO-MOF-2_{NS}** > **HNPO-MOF-2** > **HNPO-MOF-1**, and **HNPO-MOF-2_{NS}** achieved a total conversion of 82 % with 10 % yield of benzaldehyde and 69 % yield of benzoic acid (Table 1, entries 1–3). According to the photoelectrochemical measurements of **HNPO-MOF-1**, **HNPO-MOF-2** and **HNPO-MOF-2_{NS}**, they possess quite similar band gaps and band positions (Figures S28–S36). The main difference lies on the photocurrent responses where **HNPO-MOF-1** exhibits the highest photocurrent intensity (Figure S37). Nonetheless, only 40 % conversion was obtained for **HNPO-MOF-1** (Table 1, entry 1). This means the surface charge carrier density and charge separation efficiency is not the key factor affecting the reaction, while the dimension and morphology of catalysts dominate the catalytic efficiency. As well established by 2D MOF nanosheets,^[19] we therefore attribute the highest performance of **HNPO-MOF-2_{NS}** to the more accessible active sites and faster diffusion of substrate/product as compared with **HNPO-MOF-1** and **HNPO-MOF-2**. Although a vast variety of POMOFs have been reported, to our best knowledge, there is no report of 2D POMOF

nanosheets for enhanced photocatalysis. Moreover, using air as terminal oxidant also presents the advantages in cost and safety as compared with other photocatalytic systems where O₂ was most frequently applied for oxidative cleavage (Table S6).^[27] In particular, the reaction was facily driven by low-energy 10 W LED, significantly lower than the 300 W or 400 W light sources typically used for other POM-based photocatalysts in lignin β-1 and β-4 model conversion (Table S6).^[25,28]

Control experiment indicated that the precursors including **HL**, CuSO₄, {P₈W₄₈} and Na₂WO₄ or their mixture exhibited much lower conversions compared to **HNPO-MOFs** (Table S7, entries 4–8), implying the synergistic effect arisen from order arrangement of all the components into periodic frameworks.^[29] According to the Mott–Schottky plot and band gap, the LUMO and HOMO of {P₈W₄₈} are calculated to be –0.14 V and 3.09 V vs. normal hydrogen electrode (NHE), respectively (Figure S36). Although the oxidation potential of HOMO is as high as 3.09 V, only 12 % conversion and almost 100 % selectivity was observed for the product of benzaldehyde (Table S7, entry 6). The same phenomenon has been found for a series of typical semiconductors bearing high oxidation potential during photocatalytic conversion of β-1 lignin model compound, which is mainly caused by the less negative reduction potential than that to generate O₂^{•–} (–0.33 V vs. NHE), the dominant reactive oxidant for C–C bond cleavage.^[22] In contrast, the in situ transformation of {P₈W₄₈} to {W₅₈}/[W₆₄] and combination with copper sites and ligand in the skeleton of **HNPO-MOFs**, all the conduction bands of **HNPO-MOF-1**, **HNPO-MOF-2** and **HNPO-MOF-2_{NS}** are more negative than –0.33 V, thus facilitating the formation of O₂^{•–} due to the synergistic effect that endow corresponding **HNPO-MOFs** with tunable band structures (Figure S36).^[26a,30] Moreover,

Table 1: Photocatalytic Reaction of Lignin β-1 Models.^a

Entry	Substrate	Cat.	Conv. ^b (%)	Yield of Products (%)
1		HNPO-MOF-1	40	
2		HNPO-MOF-2	46	
3		HNPO-MOF-2_{NS}	82	
4		HNPO-MOF-2_{NS}	86	
5		HNPO-MOF-2_{NS}	99	
6		HNPO-MOF-2_{NS}	99	
7		HNPO-MOF-2_{NS}	99	

^aReaction conditions: substrates (0.02 mmol), Cat. (0.5 mol %), CH₃CN (2 ml), air, 400 nm LED 10 W, 30 h, room temperature. ^bConversion and yield were determined by ¹H NMR relative to the internal standard (1,3,5-trimethoxybenzene).

performing the reaction without catalyst, in the atmosphere of N_2 or in the absence of photo-irradiation gave cleavage products in very low yield or trace conversion (Table S7, entries 9–11). These results indicate that the catalyst, oxygen and light are essential for this reaction.

Under optimized reaction conditions, **HNPOMOF-2_{NS}** was further tested for the cleavage of C_α – C_β bond with a broader range of β -1 lignin model compounds (Table 1, entries 4–7). For 1,2-Diphenylethanol with p - CH_3 substituent, a similar conversion to 1,2-Diphenylethanol was achieved (Table 1, entry 4), while 1,2-diphenylpropane-1,3-diol and its derivatives yielded the corresponding aromatic aldehydes and carboxylic acids in a conversion up to 99 % (Table 1, entries 5–7). These results demonstrate that the **HNPOMOF-2_{NS}** photocatalyst is tolerant to various functional groups and highly efficient for cleavage of C_α – C_β bonds in β -1 lignin models. Upon completion of the reaction, **HNPOMOF-2_{NS}** could be facilely recovered via centrifugation and reused for three cycles with little loss of catalytic performance (Figure S43). The PXRD pattern of recovered catalyst remained almost the same as the pristine sample, demonstrating the preservation of structural integrity of **HNPOMOF-2_{NS}** (Figure S44). The stability of **HNPOMOF-2_{NS}** is further verified by the almost unchanged XPS and IR signals before and after the catalytic reaction (Figure S45–46). Moreover, filtration test revealed the reaction hardly proceeded after removing **HNPOMOF-2_{NS}**, indicating no leaking of catalyst and heterogeneous nature during the reaction (Figure S47). This is further supported by inductively coupled plasma optical emission spectrometry (ICP-OES) analysis of the filtered solution after catalysis, showing negligible amounts of metal ions (< 0.01 %) (Table S8).

To elucidate the reactive oxygen species and the role of photogenerated electrons and holes during the catalysis, control experiments were carried out by adding a series of scavengers (Table S7, entries 12–15). The addition of superoxide scavenger p -benzoquinone (BQ) significantly decreased the conversion from 86 % to 30 %, suggesting $O_2^{\bullet-}$ is important for the reaction (Table S7, entry 12). Moreover, the generation of $O_2^{\bullet-}$ upon photo-radiation is ambiguously verified by the presence of characteristic EPR signals according to 5,5-dimethyl-1-pyrroline N-oxide (DMPO)– $O_2^{\bullet-}$ adduct (Figure 5a). In contrast, little change of conversion was observed upon addition of isopropanol (IPA) as hydroxyl radical quencher (Table S7, entry 13). These results led us to conclude that $O_2^{\bullet-}$ rather than $\bullet OH$ is the reactive oxidant for C–C bond cleavage. Besides, there was an abrupt decrease in conversion to 40 % by use of $AgNO_3$ as photo-generated electrons (e^-) scavenger, while the reaction was almost completely suppressed by addition of KI as the photo-generated holes (h^+) scavenger (Table S7, entries 14–15), indicating both e^- and h^+ were involved in the catalytic process.

Based on the above results and previous reports, the plausible mechanism is proposed for photocatalytic oxidative cleavage of C–C bond in lignin models (Figure 5c). Under visible light irradiation, electron-hole pairs are effectively generated and separated. Since the LUMO of **HNPOMOF-2_{NS}** is more negative than -0.33 V (Figure 5b),

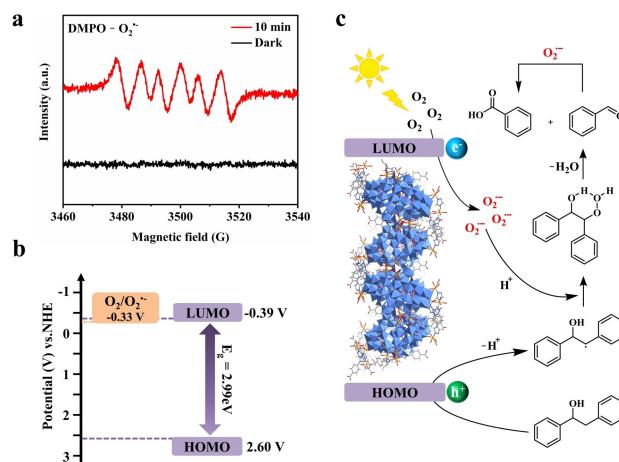


Figure 5. (a) EPR signals of the radical adduct between DMPO and $O_2^{\bullet-}$ from irradiation of **HNPOMOF-2_{NS}** in methanol dispersion. (b) Band positions of **HNPOMOF-2_{NS}**. (c) Proposed mechanism for photocatalytic oxidative cleavage of C–C bond catalyzed by **HNPOMOF-2_{NS}**.

photogenerated electrons can quickly transfer from LUMO to molecular O_2 , resulting in $O_2^{\bullet-}$. Meanwhile, 1,2-Diphenylethanol will be subjected to hydrogen abstraction by hole to form a C_β radical intermediate, which then rapidly combine with $O_2^{\bullet-}$ to give a six-membered-ring transition state, leading to the cleavage of C–C bond and thereby the production of benzaldehyde. Further oxidation of benzaldehyde by $O_2^{\bullet-}$ will afford benzoic acid. This is the dominant mechanism for photocatalytic oxidation.^[20]

Conclusion

In summary, we have developed a strategy by controlling the reactivity of parent high-nuclearity POM cluster via reducing the availability of both internal and external oxo sites for self-assembly, and this has led to the synthesis of unprecedented $\{W_{58}\}$ and $\{W_{64}\}$ -based **HNPOMOF-1** and **HNPOMOF-2**. Remarkably, $\{W_{58}\}$ and $\{W_{64}\}$ are regarded as the highest POM clusters used for building MOF materials. **HNPOMOF-1** features 3D framework containing cage-like cavity defined by exposed carboxyl groups. On the other hand, the inherent 2D layer-like structure enables the facile exfoliation of **HNPOMOF-2** into ultrathin nanosheets. Compared with **HNPOMOF-1** and **HNPOMOF-2**, **HNPOMOF-2_{NS}** exhibits superior activity towards photocatalytic oxidative cleavage of C–C bond for a series of lignin models. This work demonstrates high-nuclearity clusters can act as versatile BBs for construction of porous frameworks under controlled reactivity, which can further promote the development of novel high-nuclearity cluster-based functional materials.

Acknowledgements

This work was supported by the National Natural Science Foundation of China (No. 92161111 and 21901038), the Program for Professor of Special Appointment (Eastern Scholar) at Shanghai Institutions of Higher Learning, International Cooperation Fund of Science and Technology Commission of Shanghai Municipality (No. 21130750100). We thank the staff from College of Materials Science and Engineering (Donghua University) for X-ray data collection using Bruker D8 Venture and the staff from the BL17B1 beamline of the National Facility for Protein Science in Shanghai (NFPS) at the Shanghai Synchrotron Radiation Facility, for assistance during data collection. We also gratefully acknowledge financial support from the EPSRC (no. EP/L023652/1; EP/R009902/1; EP/R020914/1; EP/R01308X/1; EP/S017046/1; EP/S019472/1; EP/V048341/1), the European Research Council (Project 670467 SMART-POM) and the University of Glasgow.

Conflict of Interest

We declare no conflict of interests.

Data Availability Statement

The data that support the findings of this study are available in the Supporting Information of this article.

Keywords: polyoxometalates • high-nuclearity cluster • porous framework • catalysis

- [1] a) C. L. Hill, *Chem. Rev.* **1998**, *98*, 1–2; b) M. T. Pope, A. Müller, in *Polyoxometalate Chemistry From Topology via Self-Assembly to Applications* (Eds.: M. T. Pope, A. Müller), Springer Netherlands, Dordrecht, **2001**, pp. 1–6; c) L. Cronin, A. Müller, *Chem. Soc. Rev.* **2012**, *41*, 7325–7648.
- [2] a) D.-L. Long, R. Tsunashima, L. Cronin, *Angew. Chem. Int. Ed.* **2010**, *49*, 1736–1758; b) L. Vilà-Nadal, L. Cronin, *Nat. Rev. Mater.* **2017**, *2*, 17054; c) W. Guan, G. Wang, B. Li, L. Wu, *Coord. Chem. Rev.* **2023**, *481*, 215039; d) X.-Q. Ma, H.-P. Xiao, Y. Chen, Q.-S. Lai, X.-X. Li, S.-T. Zheng, *Coord. Chem. Rev.* **2024**, *510*, 215818; e) A. Ebrahimi, L. Krivosudský, A. Cherevan, D. Eder, *Coord. Chem. Rev.* **2024**, *508*, 215764; f) S.-T. Zheng, J. Zhang, G.-Y. Yang, *Angew. Chem. Int. Ed.* **2008**, *47*, 3909–3913; g) Y.-R. Wang, Q. Huang, C.-T. He, Y. Chen, J. Liu, F.-C. Shen, Y.-Q. Lan, *Nat. Commun.* **2018**, *9*, 4466; h) S. Khelifi, J. Marrot, M. Haouas, W. E. Shepard, C. Falaise, E. Cadot, *J. Am. Chem. Soc.* **2022**, *144*, 4469–4477; i) M.-M. Wang, J.-J. Cai, H.-J. Lun, M.-G. Lv, J.-Q. Zhang, S. Andra, B. Li, D.-B. Dang, Y. Bai, Y.-M. Li, *Adv. Funct. Mater.* **2024**, *34*, 2311912; j) B. Nohra, H. El Moll, L. M. Rodriguez Albello, P. Mialane, J. Marrot, C. Mellot-Draznieks, M. O’Keeffe, R. Ngo Biboum, J. Lemaire, B. Keita, L. Nadjo, A. Dolbecq, *J. Am. Chem. Soc.* **2011**, *133*, 13363–13374; k) C.-Y. Sun, S.-X. Liu, D.-D. Liang, K.-Z. Shao, Y.-H. Ren, Z.-M. Su, *J. Am. Chem. Soc.* **2009**, *131*, 1883–1888.
- [3] R. Contant, A. Teze, *Inorg. Chem.* **1985**, *24*, 4610–4614.
- [4] a) B. Keita, Y. W. Lu, L. Nadjo, R. Contant, *Electrochem. Commun.* **2000**, *2*, 720–726; b) M. Ammam, B. Keita, L. Nadjo, J. Fransaer, *Sens. Actuators B* **2009**, *142*, 347–354.
- [5] a) A. Müller, M. T. Pope, A. M. Todea, H. Bögge, J. van Slageren, M. Dressel, P. Gouzerh, R. Thouvenot, B. Tsukerblat, A. Bell, *Angew. Chem. Int. Ed.* **2007**, *46*, 4477–4480; b) S. S. Mal, M. H. Dickman, U. Kortz, A. M. Todea, A. Merca, H. Bögge, T. Glaser, A. Müller, S. Nellutla, N. Kaur, J. van Tol, N. S. Dalal, B. Keita, L. Nadjo, *Chem. Eur. J.* **2008**, *14*, 1186–1195; c) P. Yang, M. Alsufyani, A.-H. Emwas, C. Chen, N. M. Khashab, *Angew. Chem. Int. Ed.* **2018**, *57*, 13046–13051; d) Y. Koizumi, K. Yonesato, S. Kikkawa, S. Yamazoe, K. Yamaguchi, K. Suzuki, *J. Am. Chem. Soc.* **2024**, *146*, 14610–14619; e) S. S. Mal, U. Kortz, *Angew. Chem. Int. Ed.* **2005**, *44*, 3777–3780; f) K. Yonesato, D. Yanai, S. Yamazoe, D. Yokogawa, T. Kikuchi, K. Yamaguchi, K. Suzuki, *Nat. Chem.* **2023**, *15*, 940–947.
- [6] a) S. G. Mitchell, C. Streb, H. N. Miras, T. Boyd, D.-L. Long, L. Cronin, *Nat. Chem.* **2010**, *2*, 308–312; b) C.-H. Zhan, Q. Zheng, D.-L. Long, L. Vilà-Nadal, L. Cronin, *Angew. Chem. Int. Ed.* **2019**, *58*, 17282–17286; c) S. G. Mitchell, D. Gabb, C. Ritchie, N. Hazel, D.-L. Long, L. Cronin, *CrystEngComm* **2009**, *11*, 36–39; d) T. Boyd, S. G. Mitchell, D. Gabb, D.-L. Long, Y.-F. Song, L. Cronin, *J. Am. Chem. Soc.* **2017**, *139*, 5930–5938.
- [7] a) H. Furukawa, K. E. Cordova, M. O’Keeffe, O. M. Yaghi, *Science* **2013**, *341*, 1230444; b) S. Horike, S. Kitagawa, *Nat. Mater.* **2017**, *16*, 1054–1055; c) B. E. R. Snyder, A. B. Turkiewicz, H. Furukawa, M. V. Paley, E. O. Velasquez, M. N. Dods, J. R. Long, *Nature* **2023**, *613*, 287–291; d) S. Krause, V. Bon, I. Senkovska, U. Stoeck, D. Wallacher, D. M. Többsens, S. Zander, R. S. Pillai, G. Maurin, F.-X. Coudert, S. Kaskel, *Nature* **2016**, *532*, 348–352.
- [8] a) A. Kirchon, L. Feng, H. F. Drake, E. A. Joseph, H.-C. Zhou, *Chem. Soc. Rev.* **2018**, *47*, 8611–8638; b) K. Wang, Y. Li, L.-H. Xie, X. Li, J.-R. Li, *Chem. Soc. Rev.* **2022**, *51*, 6417–6441; c) X. Luo, M. Zhang, Y. Hu, Y. Xu, H. Zhou, Z. Xu, Y. Hao, S. Chen, S. Chen, Y. Luo, Y. Lin, J. Zhao, *Science* **2024**, *385*, 647–651; d) A. M. Wright, M. T. Kapelewski, S. Marx, O. K. Farha, W. Morris, *Nat. Mater.* **2024**, 1–10.
- [9] D.-Y. Du, J.-S. Qin, S.-L. Li, Z.-M. Su, Y.-Q. Lan, *Chem. Soc. Rev.* **2014**, *43*, 4615–4632.
- [10] a) J. Duan, H. Shabbir, Z. Chen, W. Bi, Q. Liu, J. Sui, L. Đorđević, S. I. Stupp, K. W. Chapman, A. B. F. Martinson, A. Li, R. D. Schaller, S. Goswami, R. B. Getman, J. T. Hupp, *J. Am. Chem. Soc.* **2023**, *145*, 7268–7277; b) Z. Chen, S. M. Gulam Rabbani, Q. Liu, W. Bi, J. Duan, Z. Lu, N. M. Schweitzer, R. B. Getman, J. T. Hupp, K. W. Chapman, *J. Am. Chem. Soc.* **2024**, *146*, 7950–7955; c) Y. Benseghir, A. Lemarchand, M. Duguet, P. Mialane, M. Gomez-Mingot, C. Roch-Marchal, T. Pino, M.-H. Ha-Thi, M. Haouas, M. Fontecave, A. Dolbecq, C. Sassoey, C. Mellot-Draznieks, *J. Am. Chem. Soc.* **2020**, *142*, 9428–9438; d) S. Ahn, S. L. Nauert, C. T. Buru, M. Rimoldi, H. Choi, N. M. Schweitzer, J. T. Hupp, O. K. Farha, J. M. Notestein, *J. Am. Chem. Soc.* **2018**, *140*, 8535–8543; e) W. Xu, X. Pei, C. S. Diercks, H. Lyu, Z. Ji, O. M. Yaghi, *J. Am. Chem. Soc.* **2019**, *141*, 17522–17526; f) B. An, Z. Li, Z. Wang, X. Zeng, X. Han, Y. Cheng, A. M. Sheveleva, Z. Zhang, F. Tuna, E. J. L. McInnes, M. D. Frogley, A. J. Ramirez-Cuesta, L. S. Natrajan, C. Wang, W. Lin, S. Yang, M. Schröder, *Nat. Mater.* **2022**, *21*, 932–938; g) Y.-J. Tang, M.-R. Gao, C.-H. Liu, S.-L. Li, H.-L. Jiang, Y.-Q. Lan, M. Han, S.-H. Yu, *Angew. Chem. Int. Ed.* **2015**, *54*, 12928–12932; h) T.-Y. Dang, R.-H. Li, H.-R. Tian, W. Guan, Y. Lu, S.-X. Liu, *J. Mater. Chem. A* **2022**, *10*, 16514–16523; i) Z.-M. Zhang, T. Zhang, C. Wang, Z. Lin, L.-S. Long, W. Lin, *J. Am. Chem. Soc.* **2015**, *137*, 3197–3200; j) Q. Han, C. He, M. Zhao, B. Qi, J. Niu, C. Duan, J.

- Am. Chem. Soc.* **2013**, *135*, 10186–10189; k) X.-X. Li, Y.-X. Wang, R.-H. Wang, C.-Y. Cui, C.-B. Tian, G.-Y. Yang, *Angew. Chem. Int. Ed.* **2016**, *55*, 6462–6466; l) J. Song, Z. Luo, D. K. Britt, H. Furukawa, O. M. Yaghi, K. I. Hardcastle, C. L. Hill, *J. Am. Chem. Soc.* **2011**, *133*, 16839–16846.
- [11] a) T. Zhang, J. Jiao, K. Guo, L. Zhang, C. Zhang, Q. Han, *J. Catal.* **2024**, *429*, 115287; b) S.-Q. You, Y.-J. Dong, B.-S. Hou, M. Dong, J.-L. Tong, L.-X. Wang, X.-L. Wang, C.-Y. Sun, W. Guan, Z.-M. Su, *J. Mater. Chem. C* **2023**, *11*, 7389–7396; c) Y. Liu, L. Li, S. Meng, J. Wang, Q. Xu, P. Ma, J. Wang, J. Niu, *Inorg. Chem.* **2023**, *62*, 12954–12964; d) Q. Shen, J. Chen, X. Jing, C. Duan, *ACS Catal.* **2023**, *13*, 9969–9978; e) W. Sun, C. He, T. Liu, C. Duan, *Chem. Commun.* **2019**, *55*, 3805–3808.
- [12] a) T.-P. Hu, Y.-Q. Zhao, Z. Jagličić, K. Yu, X.-P. Wang, D. Sun, *Inorg. Chem.* **2015**, *54*, 7415–7423; b) Y.-H. Luo, B. Li, D.-E. Zhang, J.-J. Ma, L. Liu, Z.-W. Tong, *J. Coord. Chem.* **2017**, *70*, 36–43.
- [13] a) B. Hou, C. Qin, C. Sun, X. Wang, Z. Su, *CCS Chemistry* **2021**, *3*, 287–293; b) H. Xu, Y. Wu, L. Yang, Y. Rao, J. Wang, S. Peng, Q. Li, *Angew. Chem. Int. Ed.* **2023**, *62*, e202217864; c) L. Huang, L. Han, W. Feng, L. Zheng, Z. Zhang, Y. Xu, Q. Chen, D. Zhu, S. Niu, *Cryst. Growth Des.* **2010**, *10*, 2548–2552; d) M. Wu, F. Jiang, D. Yuan, J. Pang, J. Qian, S. A. Al-Thabaiti, M. Hong, *Chem. Commun.* **2014**, *50*, 1113–1115; e) M. Zhao, S. Huang, Q. Fu, W. Li, R. Guo, Q. Yao, F. Wang, P. Cui, C.-H. Tung, D. Sun, *Angew. Chem. Int. Ed.* **2020**, *59*, 20031–20036; f) Z. Wang, Y.-J. Zhu, Y.-Z. Li, G.-L. Zhuang, K.-P. Song, Z.-Y. Gao, J.-M. Dou, M. Kurmoo, C.-H. Tung, D. Sun, *Nat. Commun.* **2022**, *13*, 1802.
- [14] C. Si, X. Liu, J. Xu, J. Xu, P. Ma, Q. Han, *Inorg. Chem. Front.* **2023**, *10*, 6936–6944.
- [15] a) D.-M. Chen, W. Shi, P. Cheng, *Chem. Commun.* **2015**, *51*, 370–372; b) T. Wang, W. Mei, P. Li, Y.-L. Peng, Y. Chen, J.-G. Ma, P. Cheng, M. Fang, K. Yu, Z. Zhang, *J. Mater. Chem. A* **2022**, *10*, 22175–22181.
- [16] W. Ouellette, M. H. Yu, C. J. O'Connor, D. Hagrman, J. Zubietta, *Angew. Chem. Int. Ed.* **2006**, *45*, 3497–3500.
- [17] L. Pauling, in *Structure and Bonding in Crystals* (Eds.: M. O'Keeffe, A. Navrotsky), Academic Press, **1981**, pp. 1–12.
- [18] T. M. Ivanova, K. I. Maslakov, A. A. Sidorov, M. A. Kiskin, R. V. Linko, S. V. Savilov, V. V. Lunin, I. L. Eremenko, *J. Electron Spectrosc. Relat. Phenom.* **2020**, *238*, 146878.
- [19] a) C. Tan, K. Yang, J. Dong, Y. Liu, Y. Liu, J. Jiang, Y. Cui, *J. Am. Chem. Soc.* **2019**, *141*, 17685–17695; b) Y. Liu, L. Liu, X. Chen, Y. Liu, Y. Han, Y. Cui, *J. Am. Chem. Soc.* **2021**, *143*, 3509–3518.
- [20] C. Zhang, X. Shen, Y. Jin, J. Cheng, C. Cai, F. Wang, *Chem. Rev.* **2023**, *123*, 4510–4601.
- [21] J. Xu, P. Zhou, C. Zhang, L. Yuan, X. Xiao, L. Dai, K. Huo, *Green Chem.* **2022**, *24*, 5351–5378.
- [22] X. Wu, J. Lin, H. Zhang, S. Xie, Q. Zhang, B. F. Sels, Y. Wang, *Green Chem.* **2021**, *23*, 10071–10078.
- [23] a) H. Liu, H. Li, N. Luo, F. Wang, *ACS Catal.* **2020**, *10*, 632–643; b) T. Hou, N. Luo, H. Li, M. Heggen, J. Lu, Y. Wang, F. Wang, *ACS Catal.* **2017**, *7*, 3850–3859.
- [24] a) H. Wang, G. J. Giardino, R. Chen, C. Yang, J. Niu, D. Wang, *ACS Cent. Sci.* **2023**, *9*, 48–55; b) M. Zhang, Z. Li, Y. Feng, X. Xin, G.-Y. Yang, H. Lv, *Green Chem.* **2023**, *25*, 10091–10100.
- [25] H.-J. Lee, E. S. Cho, *ACS Sustainable Chem. Eng.* **2023**, *11*, 7624–7632.
- [26] a) Y. Liu, C. Tang, M. Cheng, M. Chen, S. Chen, L. Lei, Y. Chen, H. Yi, Y. Fu, L. Li, *ACS Catal.* **2021**, *11*, 13374–13396; b) X. Chen, H. Wu, X. Shi, L. Wu, *Nanoscale* **2023**, *15*, 9242–9255.
- [27] a) A. Rahimi, A. Azarpira, H. Kim, J. Ralph, S. S. Stahl, *J. Am. Chem. Soc.* **2013**, *135*, 6415–6418; b) J. Li, Z. Li, J. Dong, R. Fang, Y. Chi, C. Hu, *ACS Catal.* **2023**, *13*, 5272–5284.
- [28] N. Shi, Y. Ding, N. Li, F. Wen, D. Liu, *J. Environ. Chem. Eng.* **2023**, *11*, 110558.
- [29] H.-R. Tian, Y.-W. Liu, Z. Zhang, S.-M. Liu, T.-Y. Dang, X.-H. Li, X.-W. Sun, Y. Lu, S.-X. Liu, *Green Chem.* **2020**, *22*, 248–255.
- [30] K. Suzuki, N. Mizuno, K. Yamaguchi, *ACS Catal.* **2018**, *8*, 10809–10825.

Manuscript received: October 31, 2024

Accepted manuscript online: December 9, 2024

Version of record online: ■■■, ■■■

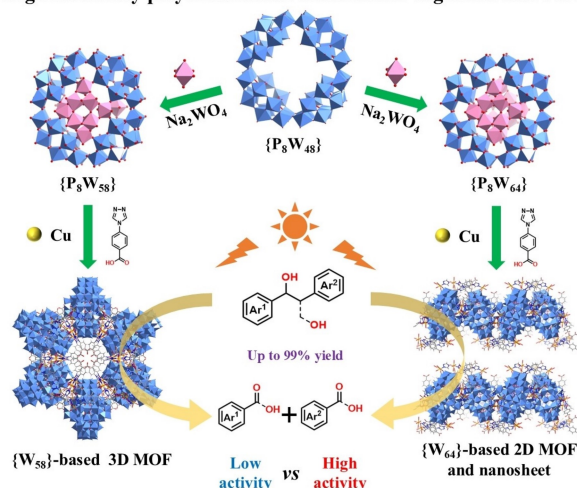
Research Article

POM-based MOFs as Photocatalysts

Q. Zhao, Y. Zeng, Z. Jiang, Z. Huang, D.-L. Long, L. Cronin,*
W. Xuan* e202421132

High-Nuclearity Polyoxometalate-Based Metal–Organic Frameworks for Photocatalytic Oxidative Cleavage of C–C Bond

High nuclearity polyoxometalate-based metal-organic framework



Two high-nuclearity polyoxometalate-based metal–organic frameworks were constructed from giant {W₅₈} and {W₆₄} via controlled stepwise assembly from {W₄₈} precursor, and the nanosheets

derived from exfoliation of 2D layer-like {W₆₄}-based MOF exhibited much enhanced activity towards photocatalytic oxidative cleavage of C–C Bond.